

## Doping in the Valley of Hydrogen Solubility: A Route to Designing Hydrogen-Resistant Zirconium Alloys

Mostafa Youssef,<sup>1</sup> Ming Yang,<sup>1</sup> and Bilge Yildiz<sup>1,2,\*</sup>

<sup>1</sup>*Department of Nuclear Science and Engineering, Laboratory for Electrochemical Interfaces, Massachusetts Institute of Technology, 77 Massachusetts Avenue, Cambridge, Massachusetts 02139, USA*

<sup>2</sup>*Department of Materials Science and Engineering, Massachusetts Institute of Technology, 77 Massachusetts Avenue, Cambridge, Massachusetts 02139, USA*

(Received 22 July 2015; revised manuscript received 17 December 2015; published 26 January 2016)

Hydrogen pickup and embrittlement pose a challenging safety limit for structural alloys used in a wide range of infrastructure applications, including zirconium alloys in nuclear reactors. Previous experimental observations guide the empirical design of hydrogen-resistant zirconium alloys, but the underlying mechanisms remain undecipherable. Here, we assess two critical prongs of hydrogen pickup through the  $ZrO_2$  passive film that serves as a surface barrier of zirconium alloys; the solubility of hydrogen in it—a detrimental process—and the ease of  $H_2$  gas evolution from its surface—a desirable process. By combining statistical thermodynamics and density-functional-theory calculations, we show that hydrogen solubility in  $ZrO_2$  exhibits a valley shape as a function of the chemical potential of electrons,  $\mu_e$ . Here,  $\mu_e$ , which is tunable by doping, serves as a physical descriptor of hydrogen resistance based on the electronic structure of  $ZrO_2$ . For designing zirconium alloys resistant against hydrogen pickup, we target either a dopant that thermodynamically minimizes the solubility of hydrogen in  $ZrO_2$  at the bottom of this valley (such as Cr) or a dopant that maximizes  $\mu_e$  and kinetically accelerates proton reduction and  $H_2$  evolution at the surface of  $ZrO_2$  (such as Nb, Ta, Mo, W, or P). Maximizing  $\mu_e$  also promotes the predomination of a less-mobile form of hydrogen defect, which can reduce the flux of hydrogen uptake. The analysis presented here for the case of  $ZrO_2$  passive film on Zr alloys serves as a broadly applicable and physically informed framework to uncover doping strategies to mitigate hydrogen embrittlement also in other alloys, such as austenitic steels or nickel alloys, which absorb hydrogen through their surface oxide films.

DOI: [10.1103/PhysRevApplied.5.014008](https://doi.org/10.1103/PhysRevApplied.5.014008)

### I. INTRODUCTION

The unwanted yet ineluctable interaction of hydrogen with metal oxides dictates the performance of these oxides in their applications by impacting their electronic [1–4] and mechanical properties [5,6]. Of focus to this paper is hydrogen pickup via zirconium oxide ( $ZrO_2$ ) followed by embrittlement in zirconium alloys which are used as cladding for the fuel in nuclear reactors. Atomic hydrogen from a variety of sources reduces the ductility and toughness of metals [7]. When a water-containing environment induces oxidative corrosion of the metal, the resulting by-product hydrogen may enter the metal from its surface. In the case of zirconium alloys, this process is regulated by a barrier oxide layer, that is,  $ZrO_2$ , which grows natively on these alloys [8]. Hydrogen embrittlement of zirconium alloys poses a safety challenge to the operation of nuclear reactors because of the reduced ability of the metal to bear a load before fracture. A fundamental understanding of the interaction of hydrogen with  $ZrO_2$  is necessary to then allow for designing utmost reliable alloys that can suppress

the source term for hydrogen entry into the underlying metal. In this work, we explain how doping  $ZrO_2$  can affect its capacity to absorb hydrogen or to discharge hydrogen gas from its surface and suggest design strategies that mitigate the ingress of hydrogen into the alloy through this barrier oxide.

Hydrogen pickup in zirconium alloys is usually expressed as the ratio between the hydrogen that enters the alloy and the total amount of hydrogen generated from the oxidation of zirconium by water. The  $ZrO_2$  layer that grows natively on zirconium alloys regulates the entry of hydrogen to the underlying alloy [8,9]. Thus, it is anticipated that the impact of the alloying elements on hydrogen pickup takes place via the  $ZrO_2$  layer. The 3d transition metals that have been traditionally used for alloying zirconium have limited solubility in this metal, and they tend to precipitate as intermetallic compounds. Both the dissolved and precipitated components of the transition metals are oxidized progressively as they become part of the  $ZrO_2$  layer [10], and so they provide a source for transition-metal defects in the  $ZrO_2$  lattice. Protons are produced upon the splitting of water at the  $ZrO_2$ /water interface [11]. This is followed by two competing scenarios. In the first, protons at the surface are incorporated into

\*Corresponding author.  
byildiz@mit.edu

and diffuse through  $\text{ZrO}_2$  in the form of various hydrogen defects and eventually reach the underlying alloy—this is the detrimental outcome. In the second scenario, electrons generated by the oxidation of the underlying alloy transport through  $\text{ZrO}_2$  and transfer to the protons to reduce them at the surface, and eventually they evolve as  $\text{H}_2$  molecules—this is the desired outcome to avoid hydrogen ingress into the metal. On the other hand, electron transport across  $\text{ZrO}_2$  is thought to be the slowest process in zirconium corrosion [12]; therefore, it can decide the competition between hydrogen pickup and  $\text{H}_2$  gas evolution.

In this study, we combine density-functional theory (DFT) and thermodynamic analysis [13] to model the solubility of hydrogen in the oxide bulk and the ability to transfer electrons at the surface of monoclinic  $\text{ZrO}_2$  ( $M\text{ZrO}_2$ ) as a function of dopant elements under oxygen-rich conditions (representative of the oxide/water interface). By incarnating the chemical potential of electrons,  $\mu_e$ , as a physical descriptor for hydrogen solubility and electron availability in  $\text{ZrO}_2$ , we calculate a general hydrogen-solubility curve as a function of  $\mu_e$  for doped  $\text{ZrO}_2$ . The resulting curve has a valley shape. In the limit of noninteracting defects, we can map onto this solubility curve any compositions of doped  $\text{ZrO}_2$ . The valley of hydrogen solubility in  $\text{ZrO}_2$  provides design strategies for zirconium alloys either based on the minimum hydrogen solubility in  $M\text{ZrO}_2$  (by Cr doping) or based on the maximum achievable kinetics of proton reduction at the surface of  $M\text{ZrO}_2$  (by Nb, Ta, Mo, W, or P doping). As another utility of this solubility curve, we show that hydrogen solubility in doped  $\text{ZrO}_2$  exhibits a volcanolike dependence across the 3d transition metals as dopants, in a strong similarity with the experimentally determined [14] hydrogen pickup fraction in zirconium alloys as a function of these elements. The results herein provide a physically grounded framework to study hydrogen pickup in zirconium alloys, with special attention to the passive layer's ability to dissolve hydrogen and to reduce protons.

The framework and the physical descriptor presented here to analyze the impact of doping on the resistance of the surface oxide layer against hydrogen penetration into the underlying metal have broader applicability than the  $\text{ZrO}_2/\text{Zr}$ -alloy system. All refractory metallic alloys develop a protective corrosion layer at their surface, such as Cr-, Fe-, and Ni-oxide layers on steels and Ni-based alloys. There is evidence that these surface oxide layers affect the penetration of hydrogen into the underlying metal [15], and as such we propose that they can be engineered by doping to resist hydrogen entry. By computing the formation free energies of all hydrogen defects in these oxides, it is possible to determine general hydrogen-solubility curves as a function of  $\mu_e$  in these oxides. Here we show that this general solubility curve has a valley shape in  $\text{ZrO}_2$  thanks to having both a positive and a negative predominant hydrogen defect as we detail below. But, in other surface oxides, this

curve could have a different shape—be monotonically increasing, monotonically decreasing, or exhibiting a plateau—depending on the charge states of the predominant hydrogen defects. Based on the shape of the hydrogen-solubility curve, it is possible to propose doping schemes that minimize hydrogen entry either by reducing the solubility of hydrogen or by accelerating the proton reduction and  $\text{H}_2$  evolution at the surface of the oxide. It is, thus, possible to adopt the herein-presented framework to design corrosion layers that help in mitigating hydrogen embrittlement of metallic alloys. Contrary to the empirical doping schemes typically adopted by the industry, including the nuclear-fuel industry, our framework is informed by first-principles evaluation of defect formation free energies and employs key concepts from semiconductor physics (electron chemical potential) and catalysis (electron transfer and redox reactions) to pinpoint an effective doping strategy to resist hydrogen embrittlement.

The organization of the rest of the paper is as follows. In Sec. II, we present the methodology adopted in this work, in Sec. III, the results and discussion appear, and concluding remarks are included in Sec. IV.

## II. METHODS

### A. Structure and charge state of defects

In this study, we consider the native defects, hydrogen defects, and an alloying element (3d transition metals, Sn, Nb, Ta, W, Mo, or P) defect in monoclinic  $\text{ZrO}_2$  ( $M\text{ZrO}_2$ ). The native defects we examine are the vacancies and interstitials of both oxygen and zirconium. The initial guess for the interstitial site is the geometric center of the unit cell of  $M\text{ZrO}_2$ , and no systematic search for the lowest-energy interstitial site is conducted. The asymmetric crystal structure of  $M\text{ZrO}_2$  aids the relaxation to a reasonably low-energy configuration of the interstitial defect starting from our initial guess. Defects due to monohydrogen and dihydrogen in the interstitial site, substituting oxygen, and substituting zirconium are studied. Similar to the native interstitial defects, the initial guess for the interstitial hydrogen defect is the geometric center of the unit cell of  $M\text{ZrO}_2$ . For all dihydrogen defects, the initial guess is such that the two hydrogen species are separated by the  $\text{H}_2$  molecule bond length and oriented in the  $\langle 001 \rangle$  direction. We examine the clustering of three and four hydrogen species in zirconium vacancies [16], but we find out that hydrogen does not have a clustering tendency in the cation vacancies of the monoclinic  $\text{ZrO}_2$ . Alloying element defects considered here are expected to be present as substitutional defects on the cation sublattice. In addition to this expected site, we also examine interstitial sites (except for Mo), and in the case of P we also consider a substitution on the anion sublattice. As before, the initial guess for the interstitial alloying element defects is the geometric center of the unit cell of  $M\text{ZrO}_2$ .

For each defect, we consider multiple charge states. The minimum and maximum charge states for each elementary defect (one that is not a complex) are summarized in Supplemental Material, Sec. 1 [17]. Substitutional defects are considered as defect complexes due to association between an interstitial impurity and a native vacancy. The minimum and maximum charge states examined for each defect complex are the sum of the minima and maxima, respectively, of the charge states of the elementary defects that constitute this complex. By analyzing Bader charges and spins [18,19] of the ions surrounding the defect and examining the DFT-calculated charge density, we are able to conclude the charge states that can be stabilized on or around the defect site without electron or hole delocalization [20]. Given the large number of defects considered in this study, we limit the charge localization analysis to the defects that have a concentration greater than  $10^{-16}$  at 600 K in a range of oxygen partial pressure between 1 and  $10^{-15}$  atm. The outcome of this analysis is provided in Supplemental Material, Sec. 2 [17].

## B. Construction of Kröger-Vink diagrams

We construct the Kröger-Vink diagram for monoclinic  $ZrO_2$  codoped with hydrogen and an alloying element by applying the charge-neutrality condition to the concentrations of electronic and ionic defects. The details of the approach are described in our recent work [13,21], and here we outline the notions relevant to the current study.

The concentrations of the conduction-band electrons and valence-band holes are obtained by applying Fermi-Dirac statistics to the DFT-calculated electronic density of states of undoped  $MZrO_2$ . On the other hand, the concentrations of ionic defects are calculated by minimizing the free energy of the defect-containing crystal under the assumption of noninteracting defects. This minimization requires the free energy of the formation of the ionic defects as an input. By neglecting the stress-volume term, which is compatible with the limit of noninteracting defects, the free energy of the formation of a defect  $d$  with charge  $q$  is defined as

$$G_{d,q}^f = (E_{\text{pot}}^{\text{def}} + F_{\text{vib}}^{\text{def}}) - (E_{\text{pot}}^{\text{perf}} + F_{\text{vib}}^{\text{perf}}) + \sum_k \Delta n_k \mu_k + q(E_{\text{VBM}} + \mu_e) + E_{\text{corr}}, \quad (1)$$

where  $E_{\text{pot}}^{\text{def}}$  and  $E_{\text{pot}}^{\text{perf}}$  are the potential energies of the defective and perfect crystals, respectively. Similarly,  $F_{\text{vib}}^{\text{def}}$  and  $F_{\text{vib}}^{\text{perf}}$  are the vibrational free energies of the defective and perfect crystal, respectively.  $\Delta n_k$  is the difference between the number of ions of the species  $k$  in the perfect crystal and the number of ions of the same species in the defective crystal,  $\mu_k$  is the chemical potential of the species  $k$ ,  $E_{\text{VBM}}$  is the energy of the valence-band maximum in the perfect crystal, and  $\mu_e$  is the chemical potential of electrons

which is also known as the Fermi level. The zero of  $\mu_e$  is chosen to be coincident with  $E_{\text{VBM}}$ , and hence  $\mu_e$  ranges from zero up to the value of the band gap of the perfect crystal as calculated using DFT. For  $MZrO_2$ , the DFT-calculated band gap is 3.5 eV, which is underestimated compared to the experimental values of 4.2 eV determined using electron energy-loss spectroscopy [22] or 5.8 eV determined using ultraviolet spectroscopy [23]. In this work, if the equilibrium value for  $\mu_e$  is greater than  $E_{\text{VBM}} + \frac{1}{2}E_{\text{gap}}$  we describe  $MZrO_2$  as  $n$ -type doped, whereas if  $\mu_e$  is less than  $E_{\text{VBM}} + \frac{1}{2}E_{\text{gap}}$ ,  $MZrO_2$  is considered to be  $p$ -type doped. Finally,  $E_{\text{corr}}$  is a correction to account for simulating charged defects in a finite supercell. In this work, we adopt the first-order Makov-Payne (MP1) correction [24]. In applying this correction, we use a scalar static dielectric constant of 20 as an average for the dielectric tensor which we calculate using density-functional perturbation theory [25] to be ( $\epsilon_{11} = 24$ ,  $\epsilon_{22} = 22$ ,  $\epsilon_{33} = 18$ ,  $\epsilon_{13} = 1$ ). Our calculations of the dielectric tensor are in line with prior theoretical work [26,27]. Inspecting the tensor shows that the off-diagonal terms are very small and the diagonal terms are almost isotropic. This justifies using a scalar dielectric constant in applying the Makov-Payne correction. Moreover, it is shown for the fully ionized anion and cation vacancy in the isostructural and chemically similar monoclinic  $HfO_2$  that the anisotropy in the dielectric tensor has a negligible effect on the value of the charged supercell correction [28]. In Sec. 3 of Supplemental Material [17], we compare the performance of the MP1 correction to the computationally expensive finite-size scaling correction [29] for selected defects. With respect to the finite-size scaling correction, the maximum error for the MP1-corrected formation energies is found to be  $-0.51$  eV in the case of  $V_{\text{Zr}}^{\text{IV}}$ . On the other hand, the uncorrected results have a maximum error of  $-2.06$  eV with respect to finite-size scaling. In general, the MP1 correction is found to improve the uncorrected formation energies. While not perfect, the MP1 correction is suitable for this study, which considers a large number of defects, and it also reduces the error in electrostatics to within the range of other uncertainties such as the approximate DFT exchange correlation and the harmonic approximation for phonons.

It remains to clarify the values of the chemical potential of species  $\mu_k$  used in Eq. (1). For the native defects, all that is needed is the chemical potential of oxygen  $\mu_{\text{O}}$  from which the chemical potential of zirconium  $\mu_{\text{Zr}}$  can be deduced [13,16]. For every Kröger-Vink diagram,  $\mu_{\text{O}}$  is allowed to vary in a range that corresponds to a range of oxygen partial pressure,  $P_{\text{O}_2}$ , from 1 to  $10^{-15}$  atm. The defect equilibrium at  $P_{\text{O}_2} = 1$  atm is considered to be representative of the oxygen-rich part of  $ZrO_2$ , that is, the surface of  $ZrO_2$  interfacing with water in the nuclear reactor (see also Secs. 12 and 14 in Supplemental Material [17]).  $\mu_{\text{O}}$  is obtained from  $P_{\text{O}_2}$  as



$$\begin{aligned} \mu_{\text{O}}(T, P_{\text{O}_2}) &= \frac{1}{2} \left[ E_{\text{O}_2}^{\text{DFT}} + E_{\text{over}} + \mu_{\text{O}_2}^0(T, P^0) + k_B T \ln \left( \frac{P_{\text{O}_2}}{P^0} \right) \right], \end{aligned} \quad (2)$$

where  $E_{\text{O}_2}^{\text{DFT}}$  is the calculated DFT energy of the oxygen molecule and  $E_{\text{over}}$  is a correction for the  $\text{O}_2$  overbinding error caused by DFT. The details of obtaining this correction following the scheme proposed by Wang, Maxisch, and Ceder [30] are described in Supplemental Material, Sec. 4 [17].  $\mu_{\text{O}_2}^0(T, P^0)$  is a reference chemical potential for  $\text{O}_2$  gas at a reference pressure  $P^0$ , which is typically 1 atm.  $\mu_{\text{O}_2}^0(T, P^0)$  is obtained from tabulated thermochemical data [31]. Hydrogen defects require a value for the chemical potential of hydrogen  $\mu_{\text{H}}$ , which in this work is computed as

$$\mu_{\text{H}}(T) = \frac{1}{2} [\mu_{\text{H}_2\text{O}}(T, P_{\text{H}_2\text{O}} = 1 \text{ atm}) - \mu_{\text{O}}(T, P_{\text{O}_2} = 1 \text{ atm})], \quad (3)$$

where  $\mu_{\text{H}_2\text{O}}$  is calculated from  $P_{\text{H}_2\text{O}}$  using an equation similar to Eq. (2) except for the overbinding error, which does not apply to the  $\text{H}_2\text{O}$  molecule. The choice of a  $\mu_{\text{H}}$  dependent only on temperature in Eq. (3) represents the situation where water is located only at the oxygen-rich part of the oxide (water/ $M\text{ZrO}_2$  interface) and provides the source term for all hydrogen defects throughout the oxide layer. Finally, the chemical potential of a transition metal (or any alloying element)  $\mu_M$  is computed as

$$\mu_M(T, P_{\text{O}_2}) = \frac{y}{x} \left[ \frac{1}{y} \mu_{M_x\text{O}_y} - \mu_{\text{O}}(T, P_{\text{O}_2}) \right], \quad (4)$$

where  $\mu_{M_x\text{O}_y}$  is the chemical potential of the metal oxide  $M_x\text{O}_y$  which is taken to be the DFT-calculated energy for the chemical formula of this oxide. The choice of both  $T$  and a  $P_{\text{O}_2}$ -dependent chemical potential for the alloying element is consistent with the situation taking place in the zirconium alloy in the nuclear reactor. In this alloy, the transition metal exists initially both dissolved in the alloy and as an intermetallic precipitate. Upon oxidation, these two components serve as the source term for the transition-metal defects in zirconia. Since these alloying metals are distributed throughout the zirconium alloy, it is expected to be present throughout the zirconia layer and hence exposed to the gradient of the chemical potential of oxygen across the zirconia film as it grows. This justifies the aforementioned choice for  $P_{\text{O}_2}$  and  $T$  dependence of  $\mu_M$ . More details about the reference oxides,  $M_x\text{O}_y$ , and discussion about the uncertainties in choosing the suitable reference are given in Supplemental Material Sec. 5 [17].

At a given equilibrium thermodynamic state, herein defined by  $T$  and  $P_{\text{O}_2}$ , we seek a unique and physically meaningful value of  $\mu_e$  that forces the concentrations of ionic and electronic defects to achieve charge neutrality [13]. By physically meaningful, we mean a value of  $\mu_e$  which does not give rise to a negative formation energy of any defect and which is bounded by the edges of the valence band and conduction band [32]. By determining this unique  $\mu_e$  value at every state, the Kröger-Vink diagram can be constructed. In this study, we construct the Kröger-Vink diagrams of  $M\text{ZrO}_2$  codoped with hydrogen and an alloying element at 600 K, which is a typical nuclear-reactor operation temperature, whereas  $P_{\text{O}_2}$  is varied between 1 and  $10^{-15}$  atm. We validate our predictions for the undoped oxide against the experimental findings as discussed in Sec. III A. The calculated formation energies for all defects and the Kröger-Vink diagrams for codoped  $M\text{ZrO}_2$  are provided in Sec. 6 of Supplemental Material [17].

Nb and Ta have high solubility in  $\text{ZrO}_2$ , and the approach of noninteracting defects is inadequate to describe them at their equilibrium solubility levels in  $\text{ZrO}_2$ . The negative formation energies found here for some of their defects in  $\text{ZrO}_2$  is direct evidence for such a high solubility for these elements. In this work, we overcome this issue by solving the charge-neutrality condition while constraining the solution at a fixed doping level for Nb and Ta. That is to say, we force the sum of the concentrations of their defects in  $\text{ZrO}_2$  to yield an *a priori* fixed doping level. In doing so, we made sure that this fixed doping level corresponds to a dopant chemical potential less than that which leads to the solubility limit of these elements in  $\text{ZrO}_2$ . Furthermore, we make sure that this fixed doping level corresponds to positive formation energies for all the defects. Contrary to Nb and Ta, the elements Mo, W, and P have very low solubility in  $\text{ZrO}_2$ . In their respective cases, we also solve the charge-neutrality condition by assigning a fixed doping level which is much higher than their solubility limit. In doing this, we acknowledge that the results do not represent an equilibrium solution. Instead, it is more representative of a nonequilibrium situation in which these elements are forced to dissolve in  $\text{ZrO}_2$ . Such a nonequilibrium situation could be enabled by dissolution under irradiation or by other metastable material processing routes [33].

### C. Density-functional-theory calculations

We perform density-functional-theory calculations using the projector-augmented plane-wave method [34] as implemented in the code Vienna *Ab initio* simulation package (VASP) [35–38]. For every element in this study, a number of electrons are treated as core and hence frozen, while the rest are treated as valence electrons. In Sec. 7 of Supplemental Material [17], we provide a list of the number of valence electrons for each element. The exchange correlation is treated using the standard Perdew, Burke,

and Ernzerhof (PBE) functional [39,40]. Although there is a tendency to prefer hybrid functionals that incorporate a fraction of the exact exchange in studying materials with an electronic band gap, we find out that adopting a standard PBE functional is a reasonable and optimal choice for the current study for three reasons. First, PBE is generally criticized for underestimating band gaps, and a typical remedy for this would be to employ an empirical on-site Coulomb interaction (the so-called DFT +  $U$  approach) to reproduce the experimental band gap. However, it turns out that hybrid functionals suffer a similar issue where one needs to tune the mixing and screening parameters to attain a desired band gap. For example, we use the screened hybrid functional of Heyd, Scuseria, and Ernzerhof (HSE) [41,42] with the standard 25% mixing of the exact screened exchange and a screening parameter of  $0.2 \text{ \AA}^{-1}$  and obtain a single-particle Kohn-Sham band gap of 4.51 eV for  $MZrO_2$  and a difference between the ionization potential ( $I$ ) and electron affinity ( $A$ ) of  $I - A = 5.18 \text{ eV}$  for the same oxide. Ramprasad *et al.* [43] show that, by tuning the mixing and screening parameters of the HSE functional, the band gap of  $MZrO_2$  can be varied between 4.5 and 6.5 eV. Given the wide scatter in the experimentally determined band gaps of  $MZrO_2$  (4.2–5.8 eV) [22,23], we believe that empiricism is uncalled for here and resorting to standard functionals is reasonable. In Sec. 8 of Supplemental Material [17], we attempt to apply a rigid shift of the conduction band on top of the PBE band gap and show that this leads to inaccurate defect equilibria for undoped  $MZrO_2$ . Second, PBE is criticized for favoring delocalized electrons (or holes) due to the convexity of the PBE energy as a function of the continuous fractional occupation number whereas the correct dependence is a straight line [44,45]. For  $MZrO_2$  treated using PBE and for the purpose of this study, we find out that this issue is not severe as we discuss in Supplemental Material, Sec. 9 [17]. It should be noted that a hybrid functional can also suffer from this localization-delocalization problem, especially if it is tuned to predict a certain band gap. Indeed, using standard HSE with the mixing and screening parameters indicated above, we obtain a single-particle Kohn-Sham gap that is different than  $I - A$  (4.51 vs 5.18 eV). This fact already hints that this functional does not predict correctly the straight-line behavior of the energy as a function of the fractional occupation number [45]. Third, in this work we study about 220 charge states for native, hydrogen, and alloying element defects and incorporate the contribution of phonons to the formation free energies for about 55 of them. Achieving such a task using a hybrid functional is formidable; hence, it is overall logical to choose PBE for this study.

All defect calculations are performed in a supercell made of  $2 \times 2 \times 2$  conventional unit cells of monoclinic  $ZrO_2$ . The lattice parameters and ionic positions in the relaxed unit cell of  $MZrO_2$  are provided in Sec. 10 of Supplemental

Material [17]. A kinetic energy cutoff of 450 eV and a  $2 \times 2 \times 2$  Monkhorst-Pack  $k$ -point mesh are used throughout the computations. Spin-polarized energy minimization without any symmetry constraints is performed up to a stopping criterion of  $1 \text{ meV}/\text{\AA}$ . Such a strict criterion is needed to avoid imaginary frequencies during the subsequent vibrational free energy calculations. To accelerate the convergence of the electronic structure, we apply a Gaussian smearing with a smearing width of 0.05 eV.

To evaluate the vibrational free energy, we compute the vibrational frequencies of the relaxed defect supercells in the harmonic approximation. In these calculations a central finite difference with a distance of  $0.008 \text{ \AA}$  is used to construct the Hessian matrix. Since these computations are very expensive, we perform them only for the defects with concentrations greater than  $10^{-16}$  at 600 K in a range of oxygen partial pressure between 1 and  $10^{-15}$  atm. For the rest of the defects, we assign a typical value for the vibrational free energy, but such an assigned value has no effect at all on the results conveyed here, since the formation energies of these defects are very high. Only the gamma point is used during the DFT calculations of the vibrational frequencies. Then the code PHONOPY [46] is used to compute the phonon density of states (DOS) using  $15 \times 15 \times 15$   $q$ -point mesh centered at the gamma point, and subsequently the harmonic vibrational free energy is computed.

In order to calculate the concentration of free electrons and holes, the electronic DOS is computed for the perfect crystal of  $MZrO_2$  using a 96-ion supercell. For this calculation, we employ a dense  $6 \times 6 \times 6$   $k$ -point mesh centered at the gamma point in combination with the tetrahedron method with Blöchl corrections [47].

### III. RESULTS AND DISCUSSION

#### A. Native defects of monoclinic $ZrO_2$

To enable a reference point of hydrogen solubility before assessing the effects of transition-metal dopants, we compute the defect equilibria in the undoped  $MZrO_2$ . For this material, we present in Fig. 1(a) the calculated Kröger-Vink diagram at 1200 K. Evaluation of the defect equilibria at such a high temperature is performed to enable comparison with experiments. The diagram shows that  $MZrO_2$  exhibits both  $p$ -type and  $n$ -type conductivity. The  $p$ -type behavior is found at high oxygen pressures  $P_{O_2}$ , where holes  $p_v$  are compensated by doubly charged oxygen interstitials  $O_i''$ . At this temperature, the transition from  $p$ -type to an  $n$ -type regime occurs at  $10^{-10}$  atm. At lower  $P_{O_2}$ , free electrons  $n_c$  predominate, and the charge compensation is accommodated by doubly charged oxygen vacancies  $V_O^{\bullet\bullet}$ , except at very low  $P_{O_2}$ , where charge compensation is achieved by singly charged oxygen vacancies  $V_O^\bullet$ .

Both the measured electrical conductivity [48,49] and oxide off-stoichiometry [50] of  $MZrO_2$  exhibit a slope of

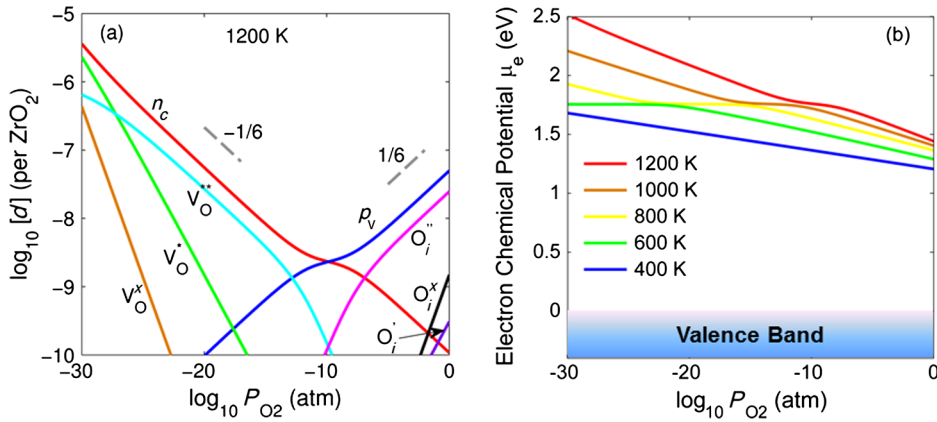


FIG. 1. (a) Calculated Kröger-Vink diagram for the undoped monoclinic  $\text{ZrO}_2$  at 1200 K. Point defects are represented by the Kröger-Vink notation,  $n_c$  denotes conduction-band electrons, and  $p_v$  denotes valence-band holes. Only defects with concentrations  $[d]$  greater than  $10^{-10}$  per  $\text{ZrO}_2$  are shown. The dashed lines are guide for the eye showing the slopes of  $(1/6)$  and  $(-1/6)$ . (b) Calculated chemical potential of electrons that achieves charge neutrality in undoped monoclinic  $\text{ZrO}_2$  as a function of  $T$  and  $P_{\text{O}_2}$ .

$-1/6$  with  $\log_{10} P_{\text{O}_2}$  at low values of  $P_{\text{O}_2}$  and at temperatures as high as 1200 K. The forgone conclusion based on these experiments is that the  $-1/6$  slope at low  $P_{\text{O}_2}$  is due to the equilibrium established between free electrons and  $V_{\text{O}}^{\bullet}$ . Our theoretical predictions are in accordance with this conclusion. On the other hand, there is no experimental consensus on the slope that conductivity or off-stoichiometry exhibit with  $\log_{10} P_{\text{O}_2}$  at high values of  $P_{\text{O}_2}$ . The experiments of Refs. [48,50] show a slope of  $1/5$ , which is interpreted as an equilibrium between holes and  $V_{\text{Zr}}^{\bullet}$ . On the other hand, a slope of  $1/4$  is found in the electrical conductivity measurements of Ref. [49], and this is attributed to the compensation between holes and singly charged interstitial oxygen  $\text{O}_i^{\bullet}$ . The discrepancy in the

experimental findings could be, in part, due to the differences among the impurities within the samples. The role of these impurities becomes more pronounced at high  $P_{\text{O}_2}$ , since the intrinsic defect concentrations are lower in that range. Our calculations reveal another complicating factor in the high- $P_{\text{O}_2}$  region. At high temperatures, the predominant defects in the high- $P_{\text{O}_2}$  region are free holes and  $\text{O}_i^{\bullet}$  as in Fig. 1(a). However, at temperatures lower than 800 K, the free holes are compensated by  $V_{\text{Zr}}^{\bullet}$  as shown in Fig. 2(a), below which is evaluated at 600 K. This change in the charge-compensation mechanism can obstruct the accurate determination of the slope of either conductivity or off-stoichiometry at high  $P_{\text{O}_2}$ . According to our model and DFT formation free energies, this transition

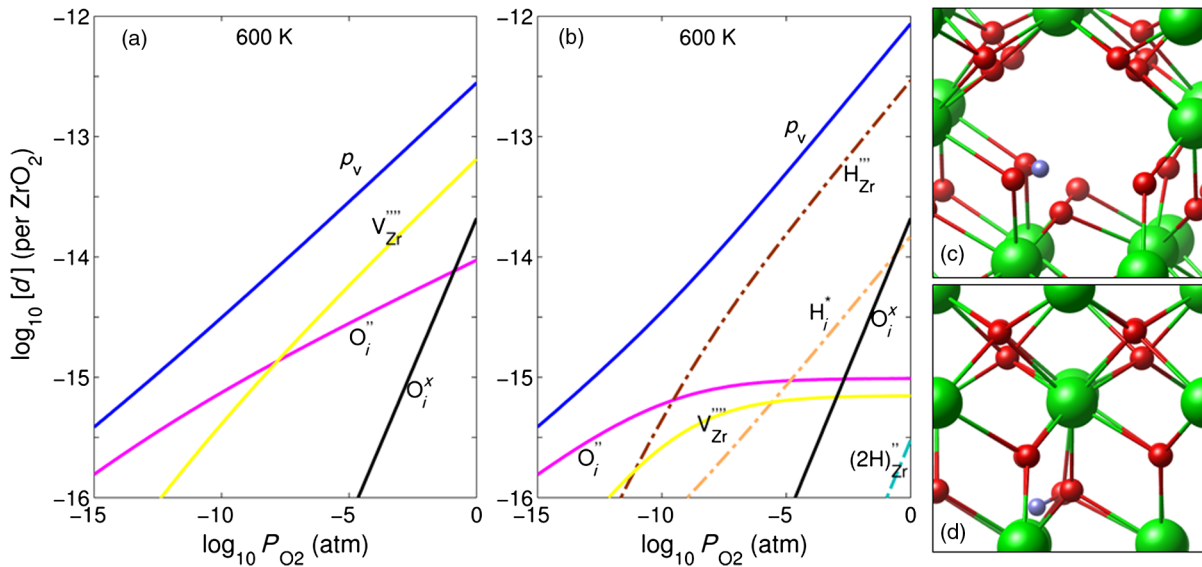


FIG. 2. Calculated Kröger-Vink diagram for undoped (a) and hydrogen-doped (b) monoclinic  $\text{ZrO}_2$ . Only the defects with concentration  $[d]$  greater than  $10^{-16}$  per  $\text{ZrO}_2$  are shown. Point defects are denoted by the Kröger-Vink notation, and  $p_v$  denotes the valence-band holes. Hydrogen defects are shown by dashed-dotted lines. In (b), the results are evaluated at  $P_{\text{H}_2\text{O}} = 1$  atm and using Eq. (3) for the chemical potential of hydrogen. (c) The relaxed structure of the complex formed between a hydrogen and a zirconium vacancy in the 3- charge state,  $\text{H}_{\text{Zr}}^{\bullet\bullet\bullet}$ . (d) The relaxed structure of the interstitial proton,  $\text{H}_i^{\bullet}$ . In (c) and (d), green (large), red (medium), and blue (small) balls represent zirconium, oxygen, and hydrogen, respectively. The visualizations in (c) and (d) are generated using the software VESTA [51].



in charge compensation is the net outcome of three competing factors. By isobaric heating above 800 K, the chemical potential of electrons  $\mu_e$  increases as shown in Fig. 1(b), the oxygen chemical potential decreases, and the change in vibrational free energy favors forming oxygen interstitials (see Figs. S4 and S5 in Supplemental Material [17]). The second and third factors win, and they favor forming  $O_i''$ . However, it is important to note that this quantitative description of the change in the charge-compensation mechanism depends on the accuracy of DFT-calculated formation free energies as discussed in the Methods section and Secs. 4 and 9 of Supplemental Material [17].

Figure 1(b) shows the calculated  $\mu_e$  that achieves charge neutrality in dopant-free  $MZrO_2$  as a function of  $T$  and  $P_{O_2}$ . For all the temperatures depicted in the figure and at 1 atm,  $MZrO_2$  is clearly in the  $p$ -type region (the middle of the DFT-predicted band gap is at 1.75 eV). Decreasing  $P_{O_2}$  isothermally leads to a gradual  $n$ -type self-doping via the native oxygen vacancies of the oxide. As indicated in the Methods section, we focus in this study on the value of  $\mu_e$  at  $P_{O_2} = 1$  atm and 600 K, which are the representative conditions for the oxygen-rich part of  $ZrO_2$  in an operative nuclear reactor.

### B. Defect equilibria in hydrogen-doped monoclinic $ZrO_2$

The impact of hydrogen on the defect equilibria of otherwise undoped  $MZrO_2$  at 600 K is shown by the calculated Kröger-Vink diagram in Fig. 2(b). Hydrogen itself is regarded as a dopant in this framework. For comparison, the equilibria of the native defects in pure  $MZrO_2$  at 600 K are shown in Fig. 2(a). Out of the large number of hydrogen defects we consider (see the Methods section), only three of them are of significant concentration in high (1 atm) to mid (approximately  $10^{-15}$  atm) oxygen partial pressure  $P_{O_2}$ . These are a complex between a single hydrogen species and a zirconium vacancy in the charge state of 3-,  $H_{Zr}'''$ , an interstitial proton  $H_i^+$ , and a complex between two hydrogen species and a zirconium vacancy in the charge state of 2-,  $(2H)_{Zr}''$ . Without any other dopants in  $MZrO_2$ ,  $H_{Zr}'''$  is the main compensator for electronic holes denoted by  $p_v$  in Fig. 2. As we show below, there is a rivalry between  $H_{Zr}'''$  and  $H_i^+$  which is settled by the value of  $\mu_e$  that depends on the dopant in the oxygen-rich part of the oxide which is represented here at  $P_{O_2} = 1$  atm.

In Figs. 2(c) and 2(d), we depict the relaxed atomic configurations of  $H_{Zr}'''$  and  $H_i^+$ , respectively. In both defects, hydrogen is present as a proton attached to a threefold-coordinated oxygen ion forming a hydroxyl group. However, we refer to the  $H_i^+$  defect as an interstitial proton rather than a hydroxide ion following the convention adopted for this defect in semiconducting oxides [1]. This naming convention is justified, especially because

the proton in this defect tends to hop independently from one site to another by breaking an old hydroxyl group and forming a new one. Using the definition of Ref. [16], the calculated binding energy of the complex  $H_{Zr}'''$  is  $-2.0$  eV, indicating a strong thermodynamic stability. This implies a strong trapping and hindrance of mobility for the proton in this defect complex. More discussion about the hydrogen defects is given Supplemental Material, Sec. 11 [17].

### C. Generalized hydrogen solubility in $ZrO_2$ —The valley

For design purposes, it is convenient to plot the hydrogen solubility as a function of a physical descriptor. Here, we provide a generalized dependence of hydrogen solubility on  $\mu_e$ , which we designate as the physical descriptor in  $MZrO_2$ . This is done in the dilute limit without considering defect complexes of hydrogen and the other dopants in the oxide. The hydrogen solubility is calculated as the sum of the concentrations of all hydrogen defects which are, in turn, obtained from the free energy of formation of these defects at a given temperature and  $P_{O_2}$ . The resulting curves as a function of  $\mu_e$  have a *valley shape*, shown in Fig. 3(a) at three temperatures and under oxygen-rich conditions representative of the water/oxide interface. The calculated valley shape is valid over a wide range of oxygen partial pressures (Supplemental Material, Sec. 12 [17]). The implication of this curve for design is that, by tuning the dopant choice and composition, one can tune  $\mu_e$  in  $MZrO_2$ . Consequently, the impact of  $\mu_e$  is twofold: on the solubility of hydrogen in the bulk of  $MZrO_2$  and on the rate of reduction of protons at the surface of  $MZrO_2$ . These design implications are discussed specifically later.

The valley shape in Fig. 3(a) can be expected naturally based on the formation free energy plot of the two predominant hydrogen defects  $H_i$  and  $H_{Zr}$  in Fig. 3(c). At  $\mu_e$  smaller than that at the minimum of the solubility (that is, the left arm of each solubility curve),  $H_i^+$  is the dominant defect, whereas at  $\mu_e$  greater than that at the minimum of solubility (that is, the right arm),  $H_{Zr}'''$  is the dominant hydrogen defect in  $MZrO_2$ . The  $\mu_e$  at the minimum of each solubility curve in Fig. 3(a) is coincident with the  $\mu_e$  at the intersection of the formation free energy lines of these two hydrogen defects as shown in Fig. 3(c). As the temperature increases, the locus of the minimum shifts to higher values of  $\mu_e$ , because the vibrational contribution to the formation free energies favors  $H_i^+$  compared to  $H_{Zr}'''$  (see Supplemental Material, Fig. S6 [17]).

The calculated solubility curves in Fig. 3 do not span the entire DFT-calculated band gap of  $MZrO_2$  (3.5 eV); instead, they are limited to a range in which the formation energies of all native and hydrogen defects are non-negative. For example, up to 900 K only the  $p$ -type region (i.e.,  $\mu_e < E_{VBM} + \frac{1}{2}E_{gap}$ ) is accessible by doping, indicating the difficulty of  $n$ -type doping in  $MZrO_2$  at these thermodynamic conditions representative of the outer part of the oxide layer near the interface with water.

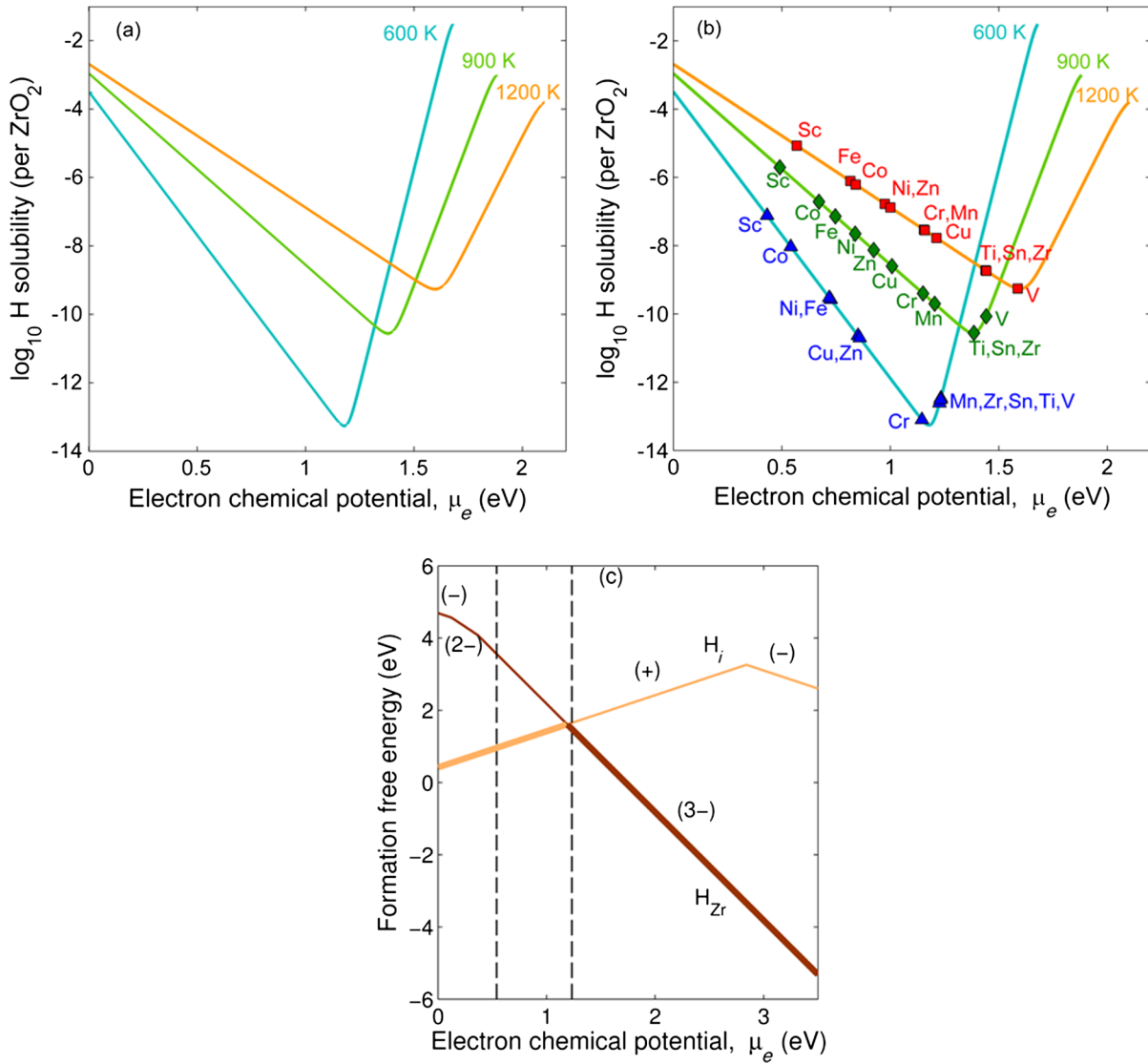


FIG. 3. (a) The calculated solubility of hydrogen in monoclinic  $\text{ZrO}_2$  as a function of the electron chemical potential ( $\mu_e$ ) at 600, 900, and 1200 K. (b) On each solubility curve, we map 11 elements for which we explicitly calculate the value of  $\mu_e$  that they establish at their solubility limit in monoclinic  $\text{ZrO}_2$  when they codope it with hydrogen. The case of  $\text{ZrO}_2$  doped with hydrogen but without any other elements is retained even at lower  $P_{\text{O}_2}$  conditions as we show in Supplemental Material, Sec. 12 [17]. (c) The formation free energy at 600 K of interstitial hydrogen,  $H_i$ , and the complex formed between hydrogen and a zirconium vacancy,  $H_{Zr}$ , as a function of  $\mu_e$ . Only the charge states of these two defects with the lowest formation free energy are shown. The thick line traces the lowest formation free energy over all hydrogen defects as a function of  $\mu_e$ . The two vertical dashed lines correspond to the range of  $\mu_e$  accessible by codoping with hydrogen and a 3d transition metal, as spanned in Fig. 4(c) from 0.54 to 1.23 eV.

Having established the general dependence of hydrogen solubility in  $M\text{ZrO}_2$  on  $\mu_e$  in Fig. 3(a), we map 11 dopants onto each isothermal solubility curve in Fig. 3(b). The loci of these dopants on the solubility curves are calculated by solving the charge-neutrality condition for the equilibrium  $\mu_e$  that these elements establish when they dissolve up to their solubility limit in  $M\text{ZrO}_2$  and codope it together with hydrogen. These 11 dopants are 3d transition metals and Sn, and their solubilities in  $M\text{ZrO}_2$  range between  $10^{-3}$  and

$10^{-14}$  per  $\text{ZrO}_2$  unit formula (see the Methods section). A subset of these 11 elements is used to develop the Zircaloy family of zirconium alloys [12]. For reference, when  $M\text{ZrO}_2$  is doped only with hydrogen, without any other metal dopant, we denote this on the curves by “Zr.” At 600 K, Cr is the dopant closest to the minimum of the hydrogen solubility in  $M\text{ZrO}_2$ . However, as the temperature increases, the distribution of the elements on the solubility valley changes due to the changes in defect



equilibria. For example, at 1200 K, V minimizes the solubility of hydrogen in  $MZrO_2$ . Next, we employ our predictions of hydrogen solubility in doped  $MZrO_2$  to provide an explanation for an intriguing empirical observation related to hydrogen pickup in zirconium alloys.

#### D. Hydrogen pickup in Zr—The volcano

A volcanolike dependence of hydrogen pickup in zirconium across the 3d transition metals that are used as alloying elements was identified in 1960 [14], as shown in Fig. 4(a). However, this empirically observed volcano behavior remains unexplained, and thereby going beyond this curve to design alloys that minimize hydrogen pickup on physical understanding has been impossible. Being the gate to the underlying metallic alloy, it is reasonable to anticipate that the capacity of the oxide layer to absorb hydrogen should exhibit a similar dependence on the 3d transition-metal dopants. Thus, we plot in Fig. 4(b) the ratio of hydrogen solubility in  $MZrO_2$  doped with a 3d transition metal to that in pure  $MZrO_2$ . These are essentially the same results in Fig. 3(b) but with the  $x$  axis recast as the dopants rather than  $\mu_e$ .

The striking feature of our resulting plot is the emergence of a volcanolike dependence of hydrogen solubility across the 3d transition-metal row. The peak is found at Co, which enhances the hydrogen solubility in  $MZrO_2$  by more than 4 orders of magnitude at the given thermodynamic conditions. Moreover, we observe that Cr reduces hydrogen solubility to 1/4 its value in the undoped oxide, whereas Ti, V, and Mn have minor effects on the solubility at these conditions. The qualitative similarity and the intuitive underlying connection between the solubility volcano

[Fig. 4(b)] and the hydrogen pickup volcano [Fig. 4(a)] are intriguing and encouraging, although the two curves do not have a one-to-one quantitative correspondence.

It is also important to clarify here that the effect of the alloying elements in Zr metal [whose nominal alloying fraction ranges between 1% and 5% in Fig. 4(a)] on hydrogen pickup is directly related to the effect of these very same elements on hydrogen solubility in  $ZrO_2$  shown in Fig. 4(b). The basis of the comparison between Figs. 4(a) and 4(b) is that the effect of the alloying elements on hydrogen pickup is mainly through the dissolution of these elements in the  $ZrO_2$  matrix. Our calculated Kröger-Vink diagrams detailed in Sec. 6 of Supplemental Material [17] indicate that in the oxygen-rich part of  $MZrO_2$  the solubility of transition metals ranges between  $10^{-3}$  and  $10^{-14}$  per  $ZrO_2$  unit formula. The rationalization of this comparison is that these alloying elements have very limited solubility in Zr metal, and as such, they form dispersed intermetallic precipitates in Zr metal leaving behind a dissolved fraction significantly lower than 1%–5% in Zr. As the oxidation front progresses, these intermetallic precipitates become part of the  $ZrO_2$  oxide, and they start to get oxidized themselves. However, these precipitates are dispersed and do not form a continuous percolated path in the host  $ZrO_2$  to allow for an uninterrupted hydrogen transport. Both the intermetallic precipitates and the alloying elements that dissolve in the Zr metal provide the source terms for the alloying elements to dope  $ZrO_2$  during oxidation. The starting total 1%–5% presence is sufficient to reach to the solubility limit of these alloying elements in  $ZrO_2$ . Consequently, the doped  $ZrO_2$  oxide layer forms a continuous path through which

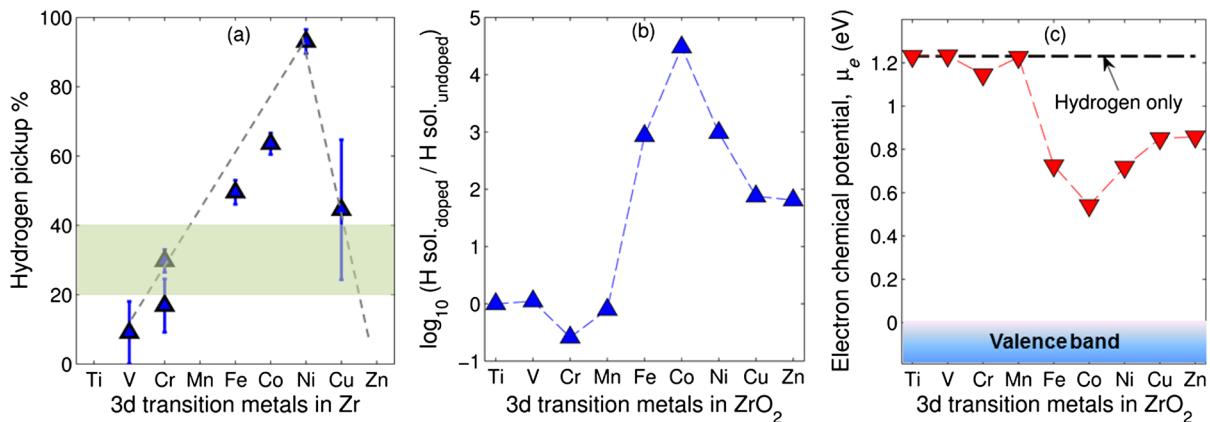


FIG. 4. (a) Experimentally determined hydrogen pickup fraction in zirconium as a function of alloying across the 3d transition-metal row. The data are based on zirconium alloys containing 1%–5% of a given transition metal and at temperatures between 573 and 773 K. The shading indicates the hydrogen pickup fraction during the oxidation of pure zirconium metal. The figure is adapted from the data in Ref. [14]. (b) The ratio of hydrogen solubility in monoclinic  $ZrO_2$  doped with 3d transition metals to that in the undoped oxide. The doping level for each metal is its equilibrium solubility in  $MZrO_2$  under the thermodynamic conditions of interest. These solubilities range between  $10^{-3}$  and  $10^{-14}$  per  $ZrO_2$  unit formula. (c) The chemical potential of electrons,  $\mu_e$ , in monoclinic  $ZrO_2$  codoped with hydrogen and a transition metal. The horizontal dashed line indicates the value of the  $\mu_e$  in the oxide doped with hydrogen only, without any transition metal. In (b) and (c), the data are evaluated at  $T = 600$  K,  $P_{O_2} = 1$  atm, and  $P_{H_2O} = 1$  atm. The effect of varying  $T$  and  $P_{O_2}$  on the volcano shape in (b) is discussed in Supplemental Material, Fig. S28 [17].

hydrogen can dissolve and transport from the water interface all the way to the underlying Zr metal. Although the solubility of 3d transition metals in  $ZrO_2$  is very small, their effect on the chemical potential of electrons and subsequently on hydrogen solubility is significant, as Fig. 4(b) testifies. Here, we do not consider the changes in the microstructure of  $ZrO_2$  due to different alloying elements. For example, Cr and Nb intermetallic precipitates would oxidize to Cr oxide and Nb oxide, respectively. Both oxides have different volumes and could lead to different stresses and strains in the surrounding  $ZrO_2$  host, affecting the local reaction and transport kinetics for hydrogen. Similarly, we do not consider the kinetics of dissolving the alloying elements into  $ZrO_2$ . Section 13 of Supplemental Material [17] elaborates more on (i) the dissolution kinetics of precipitates into the  $ZrO_2$  oxide layer, (ii) the microstructural features of the oxide that are not considered here, and (iii) the theoretical uncertainties in addressing the solubility of dopants in a metal oxide. We believe that these three factors are the main reasons for the qualitative discrepancies between the volcano of hydrogen pickup in Zr [Fig. 4(a)] and the volcano of hydrogen solubility in  $ZrO_2$  [Fig. 4(b)].

To trace the origin of the volcano shape of the predicted hydrogen solubility in Fig. 4(b), we plot in Fig. 4(c)  $\mu_e$  in  $MZrO_2$  codoped with hydrogen and a transition metal as a function of the dopants. We observe in Fig. 4(c) that Ti, V, and Mn do not introduce any noticeable change in  $\mu_e$  compared to the undoped  $MZrO_2$ , and hence they do not impact hydrogen solubility. On the other hand, the rest of the 3d transition metals introduce noticeable  $p$ -type doping to an extent that depends on the dopant metal. The equilibrium  $\mu_e$  in the case of Cr [1.15 eV in Fig. 4(c)] is the closest to the intersection between the formation free energy lines of  $H_i$  and  $H_{Zr}$ , which is at 1.19 eV in Fig. 3(c). This intersection is at the apex of the lowest possible formation free energy [traced by the thick lines in Fig. 3(c)] over all the hydrogen defects. Therefore, the solubility of hydrogen is minimal for Cr-doped  $MZrO_2$  in Fig. 4(b). Any  $p$ -type doping that lowers  $\mu_e$  below 1.19 eV increases hydrogen solubility by decreasing the formation free energy of  $H_i$ . Similarly,  $\mu_e$  above 1.19 eV increases hydrogen solubility through the  $H_{Zr}$  defects. The  $p$ -type doping is maximal in cobalt-doped  $MZrO_2$ , where  $\mu_e$  is pushed down to 0.54 eV as shown in Fig. 4(c). This explains the volcano shape around the peak of hydrogen solubility at Co in Fig. 4(b). The resulting behavior also supports the choice of  $\mu_e$  as an optimal metric to discuss the effect of an alloying element on hydrogen solubility in  $MZrO_2$  and the subsequent pickup in the underlying Zr metal. It is tempting to suggest the dominant oxidation of the alloying element in  $MZrO_2$  instead of  $\mu_e$  as the deciding factor for hydrogen solubility. However, this is not a better alternative. To explain our point, we extract from the Kröger-Vink diagrams presented in Sec. 6 of

Supplemental Material [17] the predominant oxidation state for the 3d transition metals raw in  $MZrO_2$  at  $T = 600$  K,  $P_{O_2} = 1$  atm, and  $P_{H_2O} = 1$  atm. These are  $Sc^{3+}$ ,  $Ti^{4+}$ ,  $V^{5+}$ ,  $Cr^{4+}$ ,  $Mn^{4+}$ ,  $Fe^{4+}$ ,  $Co^{4+}$ ,  $Ni^{4+}$ ,  $Cu^{3+}$ , and  $Zn^{2+}$ . If one considers the predominant oxidation state as the deciding factor for hydrogen solubility, one tends to conclude, for example, that all 4+ elements should lead to a hydrogen solubility comparable to that in pure undoped  $ZrO_2$ . The rationale here is that 4+ elements are all neutral with respect to  $Zr^{4+}$ , and as such they would not induce any changes in  $\mu_e$ . However, this is not the outcome, because, for each of these elements whose predominant oxidation state is 4+, there are also other oxidation states present but at a lower concentration. Yet, the concentration of these minority defects is still high enough to affect the  $\mu_e$  and subsequently impact the solubility of hydrogen. So if one seeks a single metric that summarizes the complex defect equilibria of  $ZrO_2$  codoped with hydrogen and an alloying element, we recommend  $\mu_e$ .

Finally, it was suggested recently based on DFT calculations that the volcano of hydrogen pickup in zirconium alloys shown in Fig. 4(a) can be explained by the effect of the alloying element on the reaction energy of the recombination of  $H^+$  and  $H^-$  at the grain boundaries of  $ZrO_2$  [52]. This explanation starting from the reduced  $H^-$  species accounts for neither the availability and transport of electrons across the insulating  $ZrO_2$  layer to reduce  $H^+$  nor the solubility of  $H^+$  in the oxide itself. Electron transport across  $ZrO_2$  is thought to be the slowest process in Zr alloy corrosion [12]; therefore, it can decide the competition between hydrogen pickup and  $H_2$  evolution. We discuss this point more in the next section.

### E. Kinetic factors: Proton reduction and hydrogen diffusion

Thus far, we focus on the thermodynamic solubility of hydrogen as a function of  $\mu_e$  that is established by the dopants in the oxide.  $\mu_e$  also enters the kinetics of hydrogen pickup by impacting the ease of proton reduction at the surface of  $ZrO_2$  and by dictating the predominant hydrogen defect,  $H_i^+$  vs  $H_{Zr}''$ . First, we start by analyzing proton reduction. For a proton to be reduced, an electron has to *transport* from the metal/oxide interface to the oxide/water interface and then it has to *transfer* from the surface of the oxide to the adsorbed proton. We believe that bulk electron transport across  $ZrO_2$  is the rate-limiting step for proton reduction. This is tentatively corroborated by the cubic kinetics observed for the overall zirconium corrosion process [12], whose cathodic reaction is the proton reduction. Had the surface electron transfer been the rate-limiting step in corrosion, linear kinetics of oxide growth with time should have been observed. Below, we discuss how  $\mu_e$  impacts electron transport, and in Sec. 15 of Supplemental Material [17] we show that changes in  $\mu_e$  due to dilute doping do not affect the rate of electron transfer at

equilibrium, since the position of the conduction-band edge at the surface of  $\text{ZrO}_2$  is not affected by dilute doping [53,54]. Electron transport can proceed via the electron or hole mechanism. However, the redox level  $\text{H}^+/\text{H}_2$  of the proton reduction is closer to the conduction band of  $\text{ZrO}_2$  at temperatures and  $\text{pH}$  of interest [55] (see Sec. 15 of Supplemental Material [17]). Therefore, the only way for  $\text{ZrO}_2$  to reduce  $\text{H}^+$  and discharge  $\text{H}_2$  gas from its surface is the transfer of electrons from its conduction band and not from its valence band. Thus, we focus the discussion below on electronic transport via the electron mechanism.

Electron transport is expected to be slowest in the oxygen-rich part of the oxide [48,49], corresponding also to the oxide surface where the reduction of protons takes place. Electron transport is quantified by the electronic conductivity  $\sigma$ , and in an insulator  $\sigma$  is proportional to the concentration of electrons in the conduction band,  $n_c$ . The latter is approximately exponentially dependent on  $\mu_e$  by the relation  $n_c \propto \exp[(\mu_e - E_{\text{CBM}})/k_B T]$ , where  $E_{\text{CBM}}$  is the energy of the conduction-band minimum. Consequently,  $p$ -type doping hinders the transport of electrons (via the electron mechanism) which are needed to reduce the adsorbed protons at the oxide/water interface. As a result, the residence time of the adsorbed protons at the surface of  $\text{ZrO}_2$  increases, and the probability of their incorporation into the oxide increases. From a design point of view, it is desirable to introduce  $n$ -type conductivity or to minimize  $p$ -type doping in  $M\text{ZrO}_2$  in order to facilitate the transport of electrons to the protons at the surface. In Fig. 5(a), we plot  $\log_{10}[\sigma(T, \mu_e)/\sigma^*(T)]$  as a function of  $\mu_e$  at three temperatures, where  $\sigma^*(T)$  is the electronic

conductivity at  $\mu_e$  that minimizes hydrogen solubility [at the dip of the valley in Fig. 3(a)], and  $\sigma(T, \mu_e)$  is the conductivity at any  $T$  and  $\mu_e$ . For the sake of simplicity, we assume exponential dependence of the conductivity on  $\mu_e$  through  $n_c$  and neglect any dopant-specific effect on the electron transport path [54]. At 600 K, a gain of 4 orders of magnitude in the electronic conductivity is achievable by maximizing  $\mu_e$ . This maximum gain in conductivity with respect to  $\sigma^*(T)$  decreases with increasing temperature.

This kinetic analysis suggests targeting an alloying element that can maximize  $\mu_e$  in the oxygen-rich part of  $M\text{ZrO}_2$  and accelerate proton reduction and  $\text{H}_2$  evolution at the surface in order to minimize the entry of hydrogen through the oxide at a given time. This kinetic acceleration of proton reduction is anticipated to impede attaining the thermodynamic limit of the absorption of hydrogen into  $M\text{ZrO}_2$ . In other words, ideally, the time to reach the thermodynamic equilibrium of hydrogen absorption can be increased beyond the time span of a corrosion cycle in the nuclear reactor (see Supplemental Material, Sec. 16 [17]).

Moreover, increasing  $\mu_e$  changes the predominant hydrogen defect from  $\text{H}_i^+$  to  $\text{H}_{\text{Zr}}^{2+}$  when  $\mu_e$  exceeds its value that minimizes the hydrogen solubility.  $\text{H}_{\text{Zr}}^{2+}$  has a binding energy of  $-2$  eV, and as such its diffusion barrier is higher than that of  $\text{H}_i^+$  by at least 2 eV. This is also a desirable effect, since it reduces the flux of hydrogen diffusing through the oxygen-rich part of the oxide. It is, however, also possible that the  $\text{H}_i^+$  effective diffusion barrier is increased due to trapping by negatively charged defects such as substitutional defects of alloying elements with oxidation state less than 4+. A future investigation would

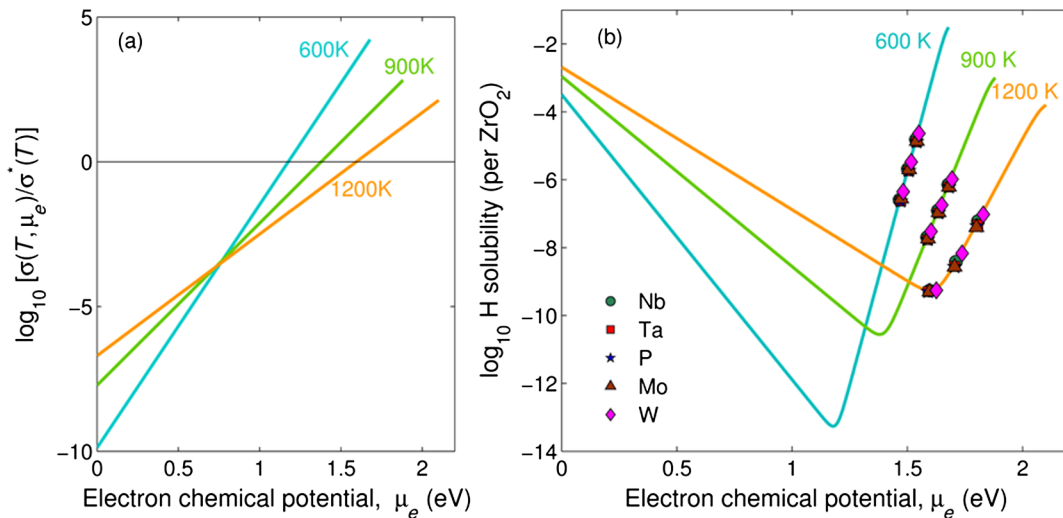


FIG. 5. (a) The ratio of the electronic conductivity  $\sigma(T, \mu_e)$  in  $M\text{ZrO}_2$  to  $\sigma^*(T)$ .  $\sigma^*(T)$  is the electronic conductivity in the same oxide at the electron chemical potential  $\mu_e$  that minimizes hydrogen solubility [the dip of the valley in Fig. 3(a) for each temperature]. (b) Mapping of five alloying elements on the hydrogen solubility curves that can maximize  $\mu_e$  in  $\text{ZrO}_2$ . On each isotherm the top data are evaluated at a fixed doping concentration by the alloying element at  $10^{-4}$  per  $\text{ZrO}_2$  unit formula, the middle data at  $10^{-5}$ , and finally the bottom data at  $10^{-6}$ . The calculations in (a) and (b) are performed assuming  $P_{\text{O}_2} = 1$  atm and  $P_{\text{H}_2\text{O}} = 1$  atm, which are representative of the oxygen-rich part of  $\text{ZrO}_2$  in contact with water.



be needed to assess whether the increase in the  $H_i^*$  effective barrier can reach up to 2 eV, similar to the trapping effect imposed by the host zirconium vacancy on  $H_{Zr}'''$ .

In order to accelerate hydrogen gas evolution and reduce the hydrogen diffusion rate in  $ZrO_2$ , we then explore doping choices that can maximize  $\mu_e$  by considering those elements that can exhibit oxidation states higher than that of  $Zr^{4+}$ . These elements are Nb, which is used in modern zirconium alloys, and Mo, P, Ta, and W, which are new dopants that were not considered before. For these elements, we force the concentration of dissolved dopants in  $ZrO_2$  to  $10^{-4}$ ,  $10^{-5}$ , and  $10^{-6}$  per  $ZrO_2$  unit formula. In Fig. 5(b), we map these potential maximizers of  $\mu_e$  on the hydrogen solubility curves. As expected, when these elements dissolve up to  $10^{-4}$  in  $ZrO_2$ , they increase the  $\mu_e$  significantly. In fact, W can achieve a larger  $\mu_e$ , because it can dissolve in the 6+ oxidation state in  $ZrO_2$  (Supplemental Material, Sec. 6 [17]).

We note here that  $10^{-4}$  is lower than the solubility limit of Ta and Nb in  $MZrO_2$ , whereas  $10^{-6}$  is much higher than the solubility of Mo, P, and W (see Sec. 6 of Supplemental Material [17]). Thus, the desirable effect of Mo, P, and W on  $\mu_e$  cannot be achieved by their thermodynamic tendency to dissolve in  $ZrO_2$ . However, the choice of these dopants is in the right direction of maximizing  $\mu_e$ , and nonequilibrium material processing techniques [33], such as those involving irradiation [56], may enable the realization of the effect of these elements on the  $ZrO_2$  electronic conductivity.

### F. Design principles against hydrogen entry

Recommendations for the design of zirconium alloys with high resistance against hydrogen pickup can be extracted from the thermodynamic and kinetic analyses

developed in the previous sections. To help in stating these recommendations, Figure 6 compiles the main results of this work. The figure shows the calculated valley-shaped hydrogen solubility as a function of  $\mu_e$  and  $T$  and depicts the temperature-dependent loci of the minimum hydrogen solubility (triangles) and the maximum attainable  $\mu_e$  (circles). These two sets of loci form the basis of the recommendations for designing zirconium alloys. In summary, we recommend targeting a dopant that either thermodynamically minimizes the solubility of hydrogen in  $ZrO_2$  (triangles) or maximizes  $\mu_e$ , kinetically accelerates proton reduction and  $H_2$  evolution at the surface, and promotes the formation of the trapped  $H_{Zr}'''$  defect (circles). Here we discuss how we arrive at these recommendations by examining three doping regimes on the hydrogen solubility valley. These are marked in Fig. 6 as (i) extreme  $p$ -type doping, (ii) doping that minimizes hydrogen solubility, and (iii) doping that maximizes  $\mu_e$ .

Our analysis shows that extreme  $p$ -type doping facilitates hydrogen pickup and so is undesirable. Such doping enhances the solubility of hydrogen in the oxide in the form of  $H_i^*$  as in zone (i), Fig. 6. In addition, this doping significantly decreases the concentration of free electrons in the oxide. This, in turn, gives sufficient residence time for the adsorbed protons on the surface of  $ZrO_2$  to be incorporated into the oxide before being reduced.

The origins of the undesirability of extreme  $p$ -type doping lead us to our first design recommendation: that is, to reduce the hydrogen solubility in the oxide by alloying zirconium with an element or a combination of elements such that, when these dissolve in  $MZrO_2$ , they establish a value for  $\mu_e$  that minimizes hydrogen solubility. This is regime (ii), marked by the triangles in Fig. 6, which spans a wide range of temperatures applicable to the

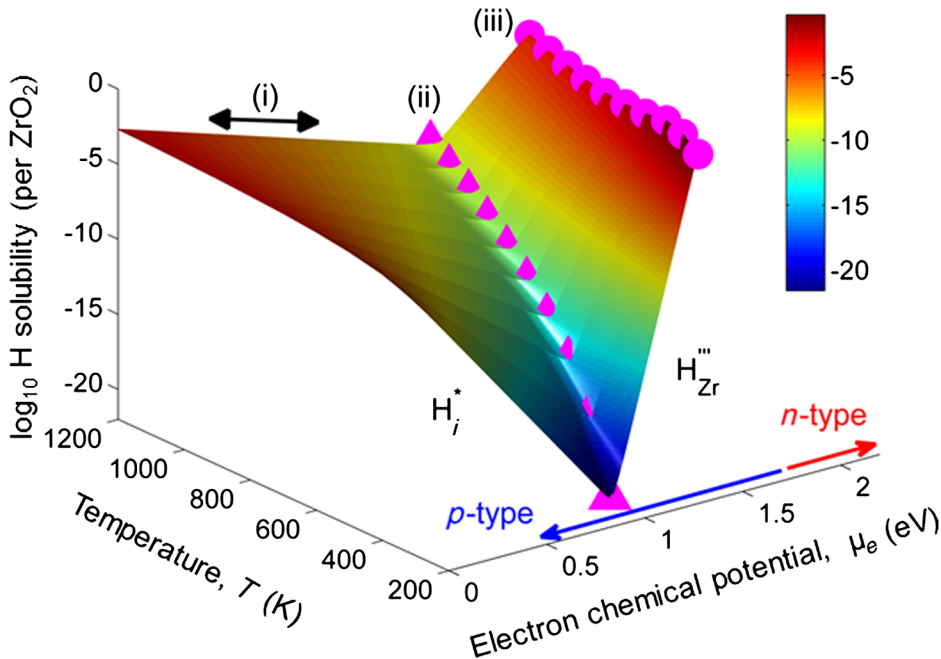


FIG. 6. The calculated hydrogen solubility in monoclinic  $ZrO_2$  as a function of electron chemical potential,  $\mu_e$  and temperature  $T$ . The temperature-dependent loci of the minimum hydrogen solubility and maximum attainable  $\mu_e$  are marked with triangles and circles, respectively. The two dominant hydrogen defects are also marked in the ranges of  $\mu_e$  over which they predominate. The zones marked by (i), (ii), and (iii) represent the three different doping strategies which are discussed in the text. These calculations are performed assuming  $P_{O_2} = 1$  atm and  $P_{H_2O} = 1$  atm, which are representative of the oxygen-rich part of  $ZrO_2$  in contact with water.

operation in the nuclear reactor and in accident conditions. At 600 K, the normal operation temperature of light water-cooled nuclear reactors, we find Cr to be an optimal element that minimizes hydrogen solubility as in Fig. 3(b). This finding is in line with the experimental observation that Cr additions can improve the resistance to hydrogen pickup [57]. The drawback of this approach is that proton reduction at the surface of  $MZrO_2$  is hindered by virtue of the insufficient amount of electrons in the oxide, because all the triangle loci in Fig. 6 lie in the  $p$ -type region of  $MZrO_2$ . Consequently, it is inevitable that some hydrogen will eventually reach the metal if this recommendation is adopted, but the advantage is that this amount is minimized.

Finally, we consider alloying zirconium with elements which can maximize  $\mu_e$  when dissolved in  $MZrO_2$  and make it lie as close as possible to the loci marked by circles [regime (iii)] in Fig. 6. We recommend such a doping approach so that the reduction of adsorbed protons by electron transfer from the surface of  $ZrO_2$  is fast by virtue of the enhancement of the electronic conductivity in the bulk of  $ZrO_2$ . In other words, the thermodynamic limit of dissolving a substantial amount of hydrogen in  $MZrO_2$  (in the form of  $H_{Zr}'''$ ) should be made very hard to attain by accelerating the proton reduction and  $H_2$  gas evolution at the surface. Ideally, the time to reach equilibrium could be made significantly longer than the time span of a corrosion cycle in the nuclear reactor. While one can kinetically fight against hydrogen absorption, when  $\mu_e$  is large it is likely that some hydrogen will still get into the oxide in the form of the  $H_{Zr}'''$  defect complex. Because this complex is strongly bound with a  $-2$  eV binding energy, it should have restricted mobility (with a migration barrier which is at least higher by 2 eV based on the binding energy of this defect, compared to a free interstitial proton). Thus, it is hard for this defect to diffuse and reach the underlying metal, another desirable factor that kinetically slows down the hydrogen pickup process at large  $\mu_e$  conditions. In Fig. 5(b), we show that Nb, Ta, Mo, P, and W can maximize  $\mu_e$  when they dissolve in  $MZrO_2$ . It is worth noting that, although these elements are able to maximize  $\mu_e$ , the actual value of  $\mu_e$  is still far from the edge of the conduction band of  $ZrO_2$  as shown in Fig. 5(b). Thus, in spite of the orders-of-magnitude enhancement in the electronic conductivity achieved with these elements in comparison to 3d transition metals, the absolute magnitude of the conductivity remains low, compatible with the wide band gap and insulating character of  $ZrO_2$ . This absolute low conductivity is desirable to maintain slow corrosion of the zirconium alloy.

Our recommendation of doping  $ZrO_2$  to maximize  $\mu_e$  is supported by recent experiments which found improved resistance to hydrogen pickup in Zr-Nb alloys compared to Zr-3d-metal alloys [8]. Those authors suggest that this improvement is due to the ability of Nb to dissolve in  $ZrO_2$  and subsequently increase the concentration of electrons in

$ZrO_2$ , but without a quantitative experimental or theoretical proof for this mechanism. In our work, we can unequivocally and quantitatively demonstrate that the improvement in the resistance to hydrogen pickup in Zr-Nb alloys is based on attaining a high  $\mu_e$  in  $ZrO_2$  when Nb dissolves into the oxide and, in turn, the easier reduction of adsorbed protons at the oxide surface followed by the discharge of  $H_2$  gas from the surface. We also show that Ta, Mo, P, and W could be possible alternatives to Nb based on performance, availability, and cost. More importantly, we provide physically justified design principles which can motivate further research for optimal compositions, for example, by considering more than one dopant element at a time.

Last, the improvement of resistance to hydrogen pickup through  $ZrO_2$  by Cr [57] (introducing  $p$ -type doping) and by Nb (introducing  $n$ -type doping) could not be reconciled prior to our work. The predictions herein of the solubility of hydrogen and the ability to reduce protons at the surface provide a unifying explanation for the way that both of these alloying elements can improve resistance of the  $ZrO_2$  passive layer against hydrogen penetration.

#### IV. CONCLUSION

In this study, we weave ideas from catalysis and semiconductor defect physics to gain insights into the mechanism of hydrogen pickup in metal alloys. This problem is detrimental in many infrastructure and energy applications of alloys in corrosive conditions, including the nuclear-energy industry. Enabled by our analysis of the charged defect equilibria in monoclinic  $ZrO_2$ , a passive oxide layer on Zr alloys, we identify the chemical potential of electrons  $\mu_e$  as a physical metric that can control the absorption of hydrogen into  $ZrO_2$ . We show that the calculated hydrogen solubility in  $ZrO_2$  exhibits a valleylike dependence on  $\mu_e$ . Thus, for designing zirconium alloys that are resistant against hydrogen pickup, we suggest two strategies that rely on tuning  $\mu_e$  by doping. We target either a dopant that thermodynamically minimizes the solubility of hydrogen in  $ZrO_2$  (such as Cr) or a dopant that maximizes  $\mu_e$  and kinetically accelerates  $H_2$  evolution at the surface of  $ZrO_2$  (such as Nb, Ta, W, P, and Mo). Maximizing  $\mu_e$  also enhances the predominance of the  $H_{Zr}'''$  defect, which is a trapped and less-mobile form of hydrogen. Moreover, we show that the computationally predicted dependence of hydrogen solubility in monoclinic  $ZrO_2$  across the row of 3d transition metals exhibits a volcanolike shape, similar to the earlier undecipherable experimental results for hydrogen pickup in zirconium across these metals.

This study provides physical and systematically quantified insights into how hydrogen absorption can depend on the composition of the native oxide film. The complexity of the microstructure [12] of the  $ZrO_2$  passive layer during the corrosion process, radiation effects [56], and kinetic factors such as the dissolution rate of alloying elements in  $ZrO_2$  and the diffusion of hydrogen in  $ZrO_2$  warrant that future

studies will add components to this framework. Hydrogen embrittlement or hydrogen-induced crack initiation is ubiquitous in many semiconducting [58,59] and metallic alloys including steels and Al- and Ni-based systems [60–64]. There is evidence that the severity of the embrittlement depends on the presence of a native oxide [15], through which hydrogen has to pass. However, there is a paucity of studying the role of the native oxides that grow on these alloys in regulating the entry of hydrogen. The approach and concepts developed in this work furnish the ground for similar studies of the oxides that grow on a broad range of structural metals that are susceptible to hydrogen embrittlement, such as steels and Ni-based alloys. Last, we believe that the computational approach presented here can also prove beneficial for the design of oxide fuel-cell materials where hydrogen reactions and proton transport are important [65].

### ACKNOWLEDGMENTS

We are grateful for the financial support from the Consortium for Advanced Simulation of Light Water Reactors (CASL), an Energy Innovation Hub for Modeling and Simulation of Nuclear Reactors under U.S. Department of Energy Contract No. DE-AC05-00OR22725, and for the computational support from National Science Foundation through the XSEDE Science Gateways program with the research allocation (TG-DMR120025). M. Yang is grateful for the MIT-China Scholarship Council (CSC) Fellowship. We thank Ju Li for helpful discussions on charged defects in oxides, Harry L. Tuller for useful insights about electron transfer, Mujid Kazimi and Alex Mieloszyk for helpful input on the role of hydrogen in the nuclear regulatory framework, and Mujid Kazimi for a critical review of the manuscript. B. Y. proposed the research. M. Y. and B. Y. designed and performed the research, discussed the results, and wrote the manuscript. M. Y. performed all the simulations except those for W, Ta, P, and Mo, which were performed by M. Yang supervised by M. Youssef and B. Y.

---

[1] C. G. Van de Walle, Hydrogen as a Cause of Doping in Zinc Oxide, *Phys. Rev. Lett.* **85**, 1012 (2000).  
 [2] A. Janotti and C. G. Van de Walle, Hydrogen multicentre bonds, *Nat. Mater.* **6**, 44 (2007).  
 [3] L. R. Merte *et al.*, Water-mediated proton hopping on an iron oxide surface, *Science* **336**, 889 (2012).  
 [4] R. Waser, Solubility of hydrogen defects in doped and undoped BaTiO<sub>3</sub>, *J. Am. Ceram. Soc.* **71**, 58 (1988).  
 [5] J. Chevalier, L. Gremillard, A. V. Virkar, and D. R. Clarke, The tetragonal-monoclinic transformation in zirconia: Lessons learned and future trends, *J. Am. Ceram. Soc.* **92**, 1901 (2009).

[6] Y.-s. Kim, Y.-h. Jeong, and S.-b. Son, A study on the effects of dissolved hydrogen on zirconium alloys corrosion, *J. Nucl. Mater.* **444**, 349 (2014).  
 [7] H. C. Rogers, Hydrogen embrittlement of metals: Atomic hydrogen from a variety of sources reduces the ductility of many metals, *Science* **159**, 1057 (1968).  
 [8] A. Couet, A. T. Motta, and R. J. Comstock, Hydrogen pickup measurements in zirconium alloys: Relation to oxidation kinetics, *J. Nucl. Mater.* **451**, 1 (2014).  
 [9] M. Harada, R. Wakamatsu, M. Limback, B. Kammenzind, and S. W. Dean, The effect of hydrogen on the transition behavior of the corrosion rate of zirconium alloys, *J. ASTM Int.* **5**, 101117 (2008).  
 [10] A. Couet, A. T. Motta, B. d. Gabory, and Z. Cai, Microbeam x-ray absorption near-edge spectroscopy study of the oxidation of Fe and Nb in zirconium alloy oxide layers, *J. Nucl. Mater.* **452**, 614 (2014).  
 [11] S. T. Korhonen, M. Calatayud, and A. O. I. Krause, Stability of hydroxylated ( $\bar{1}11$ ) and ( $\bar{1}01$ ) surfaces of monoclinic zirconia: A combined study by DFT and infrared spectroscopy, *J. Phys. Chem. C* **112**, 6469 (2008).  
 [12] B. Cox, Some thoughts on the mechanisms of in-reactor corrosion of zirconium alloys, *J. Nucl. Mater.* **336**, 331 (2005).  
 [13] M. Youssef and B. Yildiz, Intrinsic point-defect equilibria in tetragonal ZrO<sub>2</sub>: Density functional theory analysis with finite-temperature effects, *Phys. Rev. B* **86**, 144109 (2012).  
 [14] B. Cox, M. J. Davies, and A. D. Dent, *The Oxidation and Corrosion of Zirconium and its Alloys*, Part X. Hydrogen Absorption during Oxidation in Steam and Aqueous Solutions (United Kingdom Atomic Energy Authority, Harwell, 1960).  
 [15] B. P. Somerday, P. Sofronis, K. A. Nibur, C. San Marchi, and R. Kirchheim, Elucidating the variables affecting accelerated fatigue crack growth of steels in hydrogen gas with low oxygen concentrations, *Acta Mater.* **61**, 6153 (2013).  
 [16] M. Youssef and B. Yildiz, Hydrogen defects in tetragonal ZrO<sub>2</sub> studied using density functional theory, *Phys. Chem. Chem. Phys.* **16**, 1354 (2014).  
 [17] See Supplemental Material at <http://link.aps.org/supplemental/10.1103/PhysRevApplied.5.014008> for additional details and analyses about the defects considered in this study, uncertainty analysis for the valley and volcano of H solubility, discussion about the electron transfer from ZrO<sub>2</sub> surface, and discussion about the performance of standard DFT.  
 [18] R. F. W. Bader, A quantum theory of molecular structure and its applications, *Chem. Rev.* **91**, 893 (1991).  
 [19] W. Tang, E. Sanville, and G. Henkelman, A grid-based Bader analysis algorithm without lattice bias, *J. Phys. Condens. Matter* **21**, 084204 (2009).  
 [20] D. Shrader, S. M. Khalil, T. Gerczak, T. R. Allen, A. J. Heim, I. Szlufarska, and D. Morgan, Ag diffusion in cubic silicon carbide, *J. Nucl. Mater.* **408**, 257 (2011).  
 [21] U. Otgonbaatar, W. Ma, M. Youssef, and B. Yildiz, Effect of niobium on the defect chemistry and oxidation kinetics of tetragonal ZrO<sub>2</sub>, *J. Phys. Chem. C* **118**, 20122 (2014).



- [22] D. W. McComb, Bonding and electronic structure in zirconia pseudopolymorphs investigated by electron energy-loss spectroscopy, *Phys. Rev. B* **54**, 7094 (1996).
- [23] R. H. French, S. J. Glass, F. S. Ohuchi, Y. N. Xu, and W. Y. Ching, Experimental and theoretical determination of the electronic structure and optical properties of three phases of  $ZrO_2$ , *Phys. Rev. B* **49**, 5133 (1994).
- [24] G. Makov and M. C. Payne, Periodic boundary conditions in *ab initio* calculations, *Phys. Rev. B* **51**, 4014 (1995).
- [25] S. Baroni, S. de Gironcoli, A. Dal Corso, and P. Giannozzi, Phonons and related crystal properties from density-functional perturbation theory, *Rev. Mod. Phys.* **73**, 515 (2001).
- [26] J. C. Garcia, L. M. R. Scolfaro, A. T. Lino, V. N. Freire, G. A. Farias, C. C. Silva, H. W. L. Alves, S. C. P. Rodrigues, and E. F. da Silva, Structural, electronic, and optical properties of  $ZrO_2$  from *ab initio* calculations, *J. Appl. Phys.* **100**, 104103 (2006).
- [27] X. Zhao and D. Vanderbilt, Phonons and lattice dielectric properties of zirconia, *Phys. Rev. B* **65**, 075105 (2002).
- [28] Y. Kumagai and F. Oba, Electrostatics-based finite-size corrections for first-principles point defect calculations, *Phys. Rev. B* **89**, 195205 (2014).
- [29] C. W. M. Castleton, A. Höglund, and S. Mirbt, Managing the supercell approximation for charged defects in semiconductors: Finite-size scaling, charge correction factors, the band-gap problem, and the *ab initio* dielectric constant, *Phys. Rev. B* **73**, 035215 (2006).
- [30] L. Wang, T. Maxisch, and G. Ceder, Oxidation energies of transition metal oxides within the GGA + U framework, *Phys. Rev. B* **73**, 195107 (2006).
- [31] J. M. W. Chase, *NIST-JANAF Thermochemical Tables* (American Institute of Physics, Woodbury, NY, 1998).
- [32] M. Todorova and J. Neugebauer, Extending the Concept of Defect Chemistry from Semiconductor Physics to Electrochemistry, *Phys. Rev. Applied* **1**, 014001 (2014).
- [33] C. Suryanarayana, *Non-Equilibrium Processing of Materials* (Elsevier, New York, 1999), Vol. 2.
- [34] G. Kresse and D. Joubert, From ultrasoft pseudopotentials to the projector augmented-wave method, *Phys. Rev. B* **59**, 1758 (1999).
- [35] G. Kresse and J. Hafner, *Ab initio* molecular dynamics for liquid metals, *Phys. Rev. B* **47**, 558 (1993).
- [36] G. Kresse and J. Hafner, *Ab initio* molecular-dynamics simulation of the liquid-metal–amorphous-semiconductor transition in germanium, *Phys. Rev. B* **49**, 14251 (1994).
- [37] G. Kresse and J. Furthmüller, Efficiency of *ab-initio* total energy calculations for metals and semiconductors using a plane-wave basis set, *Comput. Mater. Sci.* **6**, 15 (1996).
- [38] G. Kresse and J. Furthmüller, Efficient iterative schemes for *ab initio* total-energy calculations using a plane-wave basis set, *Phys. Rev. B* **54**, 11169 (1996).
- [39] J. P. Perdew, K. Burke, and M. Ernzerhof, Generalized Gradient Approximation Made Simple, *Phys. Rev. Lett.* **77**, 3865 (1996).
- [40] J. P. Perdew, K. Burke, and M. Ernzerhof, Generalized Gradient Approximation Made Simple, *Phys. Rev. Lett.* **78**, 1396 (1997).
- [41] J. Heyd, G. E. Scuseria, and M. Ernzerhof, Hybrid functionals based on a screened Coulomb potential, *J. Chem. Phys.* **118**, 8207 (2003).
- [42] A. V. Krugau, O. A. Vydrov, A. F. Izmaylov, and G. E. Scuseria, Influence of the exchange screening parameter on the performance of screened hybrid functionals, *J. Chem. Phys.* **125**, 224106 (2006).
- [43] R. Ramprasad, H. Zhu, P. Rinke, and M. Scheffler, New Perspective on Formation Energies and Energy Levels of Point Defects in Nonmetals, *Phys. Rev. Lett.* **108**, 066404 (2012).
- [44] J. P. Perdew, A. Ruzsinszky, G. I. Csonka, O. A. Vydrov, G. E. Scuseria, V. N. Staroverov, and J. Tao, Exchange and correlation in open systems of fluctuating electron number, *Phys. Rev. A* **76**, 040501 (2007).
- [45] P. Mori-Sánchez, A. J. Cohen, and W. Yang, Localization and Delocalization Errors in Density Functional Theory and Implications for Band-Gap Prediction, *Phys. Rev. Lett.* **100**, 146401 (2008).
- [46] A. Togo, F. Oba, and I. Tanaka, First-principles calculations of the ferroelastic transition between rutile-type and  $CaCl_2$ -type  $SiO_2$  at high pressures, *Phys. Rev. B* **78**, 134106 (2008).
- [47] P. E. Blöchl, O. Jepsen, and O. K. Andersen, Improved tetrahedron method for Brillouin-zone integrations, *Phys. Rev. B* **49**, 16223 (1994).
- [48] R. W. Vest, N. M. Tallan, and W. C. Tripp, Electrical properties and defect structure of zirconia: I, Monoclinic phase, *J. Am. Ceram. Soc.* **47**, 635 (1964).
- [49] A. Kumar, D. Rajdev, and D. L. Douglass, Effect of oxide defect structure on the electrical properties of  $ZrO_2$ , *J. Am. Ceram. Soc.* **55**, 439 (1972).
- [50] J. Xue, Nonstoichiometry and point defect structure of monoclinic and tetragonal zirconia ( $ZrO_{2+\delta}$ ), *J. Electrochem. Soc.* **138**, 36C (1991).
- [51] K. Momma and F. Izumi, VESTA 3 for three-dimensional visualization of crystal, volumetric and morphology data, *J. Appl. Crystallogr.* **44**, 1272 (2011).
- [52] M. Lindgren and I. Panas, Impact of additives on zirconium oxidation by water: Mechanistic insights from first principles, *R. Soc. Chem. Adv.* **3**, 21613 (2013).
- [53] S. R. Morrison, *Electrochemistry at Semiconductor and Oxidized Metal Electrodes* (Plenum, New York, 1984).
- [54] R. Memming, *Semiconductor Electrochemistry* (Wiley-VCH, Weinheim, 2001).
- [55] Y. Xu and M. A. A. Schoonen, The absolute energy positions of conduction and valence bands of selected semiconducting minerals, *Am. Mineral.* **85**, 543 (2000).
- [56] G. S. Was, *Fundamentals of Radiation Materials Science* (Springer, Berlin, 2007).
- [57] F. Garzarolli, R. Schumann, and E. Steinberg, in *Zirconium in the Nuclear Industry: Proceedings of the Tenth International Symposium on Zirconium in the Nuclear Industry*, ASTM STP 1245, Philadelphia, USA (ASTM International, West Conshohocken, PA, 1994), p. 709.
- [58] G. Moras, L. C. Ciacchi, C. Elsässer, P. Gumbsch, and A. De Vita, Atomically Smooth Stress-Corrosion Cleavage of a Hydrogen-Implanted Crystal, *Phys. Rev. Lett.* **105**, 075502 (2010).

- [59] S. Ogata, F. Shimojo, R. K. Kalia, A. Nakano, and P. Vashishta, Environmental effects of H<sub>2</sub>O on fracture initiation in silicon: A hybrid electronic-density-functional/molecular-dynamics study, *J. Appl. Phys.* **95**, 5316 (2004).
- [60] J. Song and W. A. Curtin, Atomic mechanism and prediction of hydrogen embrittlement in iron, *Nat. Mater.* **12**, 145 (2013).
- [61] M. Dadfarnia, P. Novak, D. C. Ahn, J. B. Liu, P. Sofronis, D. D. Johnson, and I. M. Robertson, Recent advances in the study of structural materials compatibility with hydrogen, *Adv. Mater.* **22**, 1128 (2010).
- [62] D. F. Johnson and E. A. Carter, Hydrogen in tungsten: Absorption, diffusion, vacancy trapping, and decohesion, *J. Mater. Res.* **25**, 315 (2010).
- [63] P. A. Burr, S. T. Murphy, S. C. Lumley, M. R. Wenman, and R. W. Grimes, Hydrogen solubility in zirconium intermetallic second phase particles, *J. Nucl. Mater.* **443**, 502 (2013).
- [64] R. J. Zamora, A. K. Nair, R. G. Hennig, and D. H. Warner, *Ab initio* prediction of environmental embrittlement at a crack tip in aluminum, *Phys. Rev. B* **86**, 060101 (2012).
- [65] L. Malavasi, C. A. J. Fisher, and M. S. Islam, Oxide-ion and proton conducting electrolyte materials for clean energy applications: Structural and mechanistic features, *Chem. Soc. Rev.* **39**, 4370 (2010).